RSC Advances

PAPER

View Article Online
View Journal | View Issue

Cite this: *RSC Adv.*, 2025, **15**, 25872

Facile synthesis of $CoFe_2O_4$@SiO_2 nanoparticles anchored on reduced graphene oxide for highly efficient electromagnetic wave absorption

Hechao Lu,[a] Chenyu Li,[a] Kaiwen Chen,[a] Qinting He,[a] Fang Ren,[a] Juan Wu *[ab] and Renxing Dai*[c]

Received 21st May 2025
Accepted 14th July 2025

DOI: 10.1039/d5ra03579a

rsc.li/rsc-advances

In this study, a ternary composite material composed of $CoFe_2O_4$@SiO_2 nanospheres and reduced graphene oxide (RGO) was successfully synthesized through a facile route. The composites exhibited a layered "sandwich" structure, where $CoFe_2O_4$@SiO_2 nanospheres were anchored onto the surface of RGO nanosheets. The microstructure and electromagnetic wave absorption properties of the synthesized $CoFe_2O_4$@SiO_2/RGO were systematically investigated. Results revealed that the composites possessed excellent electromagnetic wave absorption performance, with a minimum reflection loss (RL) of −27.7 dB at 13.02 GHz for a thickness of 1.8 mm. Furthermore, the composites exhibited a broad absorption bandwidth of up to 14.52 GHz (3.48–18 GHz) with reflection losses less than −10 dB over a thickness range of 1.5 to 5.0 mm, covering the S–Ku band. The enhanced absorption performance could be attributed to the optimized impedance matching and synergistic electromagnetic loss mechanisms. The $CoFe_2O_4$@SiO_2/RGO composites demonstrated balanced dielectric and magnetic loss, enabled by the effective interaction of electromagnetic parameters. These results indicate that the developed composites provide a promising candidate for high-performance microwave absorbing materials with lightweight, strong absorption, and broad bandwidth characteristics, potentially applicable in military stealth technology, electromagnetic compatibility enhancement, and ecological protection.

1. Introduction

With the accelerated advancement of contemporary science and technology, electromagnetic waves (EMWs) have witnessed unprecedented proliferation across multifarious applications. These ubiquitous oscillations form the backbone of modern communication systems, radar technologies, and medical imaging modalities, while simultaneously permeating diverse industrial sectors as indispensable operational components. However, this widespread electromagnetic utilization has engendered significant collateral effects: operational electronic instruments emit substantial electromagnetic radiation that induces detrimental interference in adjacent devices, and cumulative anthropogenic electromagnetic emissions have manifested as a novel form of ecological contamination. Currently recognized as the "fifth major environmental pollutant" following traditional contaminants (atmospheric, aquatic, solid waste, and noise pollution).[1,2] This critical situation underscores the urgent necessity for developing high-performance electromagnetic wave absorbing (EMWA) materials. These functionally engineered materials are specifically designed to attenuate electromagnetic energy through sophisticated absorption mechanisms, effectively minimizing wave reflection and scattering phenomena. Their strategic importance extends across multiple domains including military stealth technology, electromagnetic compatibility enhancement in electronic systems, and ecological protection initiatives.[3] The ongoing revolution in nanotechnology and materials science has catalyzed intensive research endeavors focused on innovative synthesis methodologies and multi-scale performance optimization strategies. Current investigations emphasize nanomaterial architecture design, multi-component heterostructure engineering, and intelligent absorption mechanisms, aiming to address the escalating demands of next-generation electromagnetic protection applications.

Electromagnetic wave (EMW) absorbing materials are typically categorized into three fundamental types based on their loss mechanisms: magnetic loss, resistive loss, and dielectric loss materials.[4–8] Among these, ferrites and graphene-based materials have emerged as prominent candidates. Ferrites demonstrate exceptional promise in EMW absorption applications owing to their material abundance, favorable

[a]Jiangsu Key Laboratory of E-waste Recycling, School of Resources and Environmental Engineering, Jiangsu University of Technology, Changzhou 213001, China. E-mail: jintanwujuan@163.com; Tel: +86-18906110982
[b]National Special Superfine Powder Engineering Research Center, Nanjing University of Science and Technology, Nanjing 210094, China
[c]Jiangsu Ambassador Tongfeng Coating Co., Ltd, Changzhou 213001, China. E-mail: dairenxing@sina.cn; Tel: +86-13606112157

dispersibility, cost-effectiveness, and balanced electromagnetic properties encompassing both dielectric and magnetic loss mechanisms. However, practical limitations including high density, poor corrosion resistance, and inadequate thermal stability restrict their broader implementation in EMW absorption applications.[9,10] Furthermore, the degradation of magnetization properties at elevated frequencies significantly compromises their high-frequency absorption performance.[11] Carbon-based materials present a compelling alternative characterized by low density, broadband absorption capabilities, and superior thermal/chemical stability.[12–14] Quan *et al.*[15] successfully fabricated thermoplastic elastomer-based EMW absorption films incorporating magnetic/dielectric biphasic components, achieving an ultra-wide effective absorption bandwidth of over 14 GHz at just 1.5 mm thickness. The research team also developed a novel three-layer impedance matching gradient film architecture. This advanced design not only realized sufficient EMW introduction but also dissipated the incident EM energy with gradually increased loss capability.[16] In complementary research, Chen *et al.*[17] reported carbonyl iron powder-reinforced TCCP composite films, which exhibited a distinct absorption peak at approximately 12.25 GHz. These materials achieved effective absorption bandwidth of 4.56 GHz (RL < −5 dB) at 1.0 mm thickness and 4.27 GHz (RL < −10 dB) at 2.3 mm thickness. Graphene, a two-dimensional carbon nanostructure with sp^2-hybridized atomic networks, has attracted particular attention as a lightweight electromagnetic wave absorber due to its structural integrity and exceptional specific surface area.[18,19] Nevertheless, pure graphene exhibits suboptimal EMW absorption efficiency owing to its exclusive reliance on dielectric loss mechanisms and unfavorable impedance matching characteristics.[20] To address these limitations, researchers have developed hybrid architectures combining reduced graphene oxide (RGO) with magnetic materials to optimize impedance matching and synergistic loss mechanisms. Notable examples include $CoFe_2O_4$/RGO nanocomposites achieving an optimal reflection loss (RL) of −11.1 dB,[21] and $NiFe_2O_4$/graphene composites demonstrating a minimum RL of −29.2 dB at 16.1 GHz.[22] Other innovative systems such as RGO/$MnFe_2O_4$/PVDF,[23] Fe_2O_3/RGO,[24] and RGO/polypyrrole hybrids[25] have further expanded the research frontier in EMW absorption and shielding. However, significant surface reflection of EMWs from these composite materials induces secondary electromagnetic pollution. In this context, SiO_2, classified as a dielectric loss material with wave-transparent properties, allows more incident EMWs to penetrate the absorber interior. This mechanism not only optimizes the material's impedance matching characteristics but also synergistically enhances electromagnetic wave absorption performance through effective dielectric loss mechanisms. The optimized impedance matching achieved through this approach serves as a critical determinant in improving wave-absorbing capabilities.[26]

To develop high-performance electromagnetic wave-absorbing materials with comprehensive advantages, contemporary researches demonstrate that strategically combining multiple electromagnetic wave-absorbing materials through special structural design has proven effective in achieving the critical performance metrics of "thin, light, wide and strong" for next-generation absorbers.[27–29] Based on this, the ternary composite nanomaterial $CoFe_2O_4$@SiO_2/RGO has been successfully designed and synthesized in this work (Fig. 1). The crystal structure, morphology and electromagnetic wave absorption properties of the composites were investigated, and the composites show excellent bandwidth of electromagnetic wave absorption properties in terms of both minimum RL and excellent absorption properties. It is believed that this composite material has a broad application prospect in the field of electromagnetic wave absorption.

2. Experimental materials and methods

2.1 Materials

The commercial graphite oxide (GO) was supplied by Nanjing Jicang Nano Technology Co., Ltd, Nanjing, China. Hydrazine monohydrate ($N_2H_4 \cdot H_2O$, 80 wt%), ferric chloride ($FeCl_3 \cdot 6H_2O$), cobalt chloride hexahydrate ($CoCl_2 \cdot 6H_2O$), ethylene glycol (EG), sodium acetate (NaAc), polyethylene glycol, ammonium hydroxide ($NH_3 \cdot H_2O$, 28 wt%), 3-aminopropyl triethoxysilane (APTES) and tetraethyl orthosilicate (TEOS) were provided by Sinopharm Chemical Reagent Co., Ltd, Shanghai, China. The sodium dodecyl benzene sulfonate (SDBS) was purchased from Shanghai Maclin Biochemical Technology Co., Ltd, Shanghai, China. All chemicals were analytical grade and could be used without further purification.

2.2 Preparation of reduced graphene oxide (RGO)

The RGO nanoparticles were prepared by a modified Hummers' method.[30] Briefly, 140 mg GO and 140 mg SDBS were dispersed in 140 mL of deionized water under ultrasonic for 30 min, then transferred into a three-necked flask. After that, 0.5 mL $N_2H_4 \cdot H_2O$ (80 wt%) was slowly added and stirred under the conditions of a water bath at 80 °C for 24 h. Upon completion of the reaction, the resultant mixture was cooled to ambient temperature, followed by filtration and sequential washing cycles (three times each) using deionized water and ethanol. The purified product was subsequently immersed in a dilute hydrochloric acid solution (pH 2).

2.3 Preparation of nanometer $CoFe_2O_4$

A precursor solution was prepared by dissolving 1.35 g $FeCl_3 \cdot 6H_2O$ and 0.7 g $CoCl_2 \cdot 6H_2O$ in 40 mL EG under ultrasonic agitation to ensure thorough homogenization. Subsequently, 1.8 g NaAc and 0.5 g of polyethylene glycol were sequentially introduced into the solution under continued sonication. The resulting mixture was transferred to a round-bottom flask and subjected to thermal conditioning at 50 °C for 1 h with mechanical stirring. The homogeneous system was then sealed in a Teflon-lined stainless-steel autoclave for hydrothermal treatment at 200 °C for 8 h. Upon cooling to room temperature, the black precipitate underwent purification through triple washing cycles with alternating deionized water and ethanol.

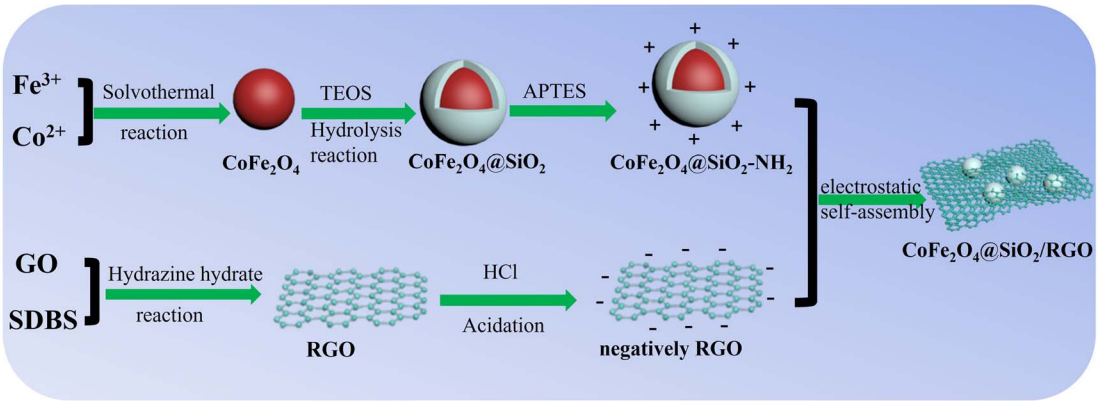

Fig. 1 Schematic illustration of the preparation of $CoFe_2O_4$@SiO_2/RGO.

Finally, the $CoFe_2O_4$ nanoparticles were dried at 45 °C under vacuum conditions.

2.4 Preparation of $CoFe_2O_4$@SiO_2/RGO composites

The preparation process of $CoFe_2O_4$@SiO_2/RGO nanocomposites, as schematically illustrated in Fig. 1, involved the following steps: 0.2 g of pre-synthesized $CoFe_2O_4$ nanoparticles were dispersed in a mixed solvent system containing 20 mL of deionized water, 1 mL $NH_3 \cdot H_2O$ (28 wt%) and 80 mL of anhydrous ethanol under ultrasonication. Then, 0.2 mL TEOS was added dropwise into the resulting system. After stirring for 12 h, 0.3 mL APTES was added. The above solution was transferred into a Teflon-lined stainless steel autoclave for hydrothermal treatment at 100 °C for 24 h. Following natural cooling, the separated solid was washed with deionized water few times. The obtained $CoFe_2O_4$@SiO_2–NH_2 composites were re-dispersed in 20 mL of deionized water to form a homogeneous suspension, whose pH was carefully adjusted to 2 using dilute HCl solution. This acidified suspension was then combined with a predetermined volume of negatively charged RGO suspension (1.5 mg mL^{-1}) under continuous stirring. After 12 h of electrostatic self-assembly, the $CoFe_2O_4$@SiO_2/RGO composites were washed with deionized water several times and then freeze-dried. As a comparison of the following research on electromagnetic wave absorption performance, $CoFe_2O_4$/RGO nanoparticles were prepared by solvothermal method. Briefly, a specific quantity of RGO was added to 40 mL EG under ultrasonication. Then, 1.35 g $FeCl_3 \cdot 6H_2O$ and 0.6 g $CoCl_2 \cdot 6H_2O$ were added under ultrasonication for 15 min. Subsequently, 1.0 g NaAc and 1.0 g of polyethylene glycol were added to the mixture. After sufficient dissolution, the homogeneous mixture was transferred to a round-bottom flask and maintained at 50 °C under mechanical stirring for 1 h. The mixture was then sealed in a 100 mL Teflon-lined stainless steel autoclave and reacted at 200 °C for 8 h. After natural cooling to the room temperature, the black precipitate was collected *via* magnetic separation. The obtained product was sequentially washed three times with deionized water and anhydrous ethanol, respectively, followed by vacuum drying at 60 °C to yield the $CoFe_2O_4$/RGO nanocomposites.

2.5 Characterizations

The morphology of synthesized samples were characterized by field-emission scanning electron microscopy (FE-SEM, Model Hitachi S-4800, Hitachi Co. Ltd, Japan) and transmission electron microscopy (TEM, Model Tecnai 12, Philips Co. Ltd, Holland). The surface elements of the samples were analyzed by energy dispersive X-ray spectrometer (EDS) attached to SEM. The crystalline phases were recorded using X-ray diffraction (XRD, Bruker Co. Ltd, Germany) with a 2θ range from 10° to 80°. Raman spectroscopy (Model LabRam II, Dilor Co. Ltd, France) was used to estimate the bond structure of RGO. The magnetic properties of the synthesized materials were detected by vibrating sample magnetometer (VSM, Model 7410, Lake Shore Co. Ltd, USA) at room temperature. The electromagnetic (EM) parameters of the $CoFe_2O_4$@SiO_2/RGO composite materials were characterized using a vector network analyzer (VNA, Model HP-8720ES, Agilent, Co. Ltd, USA) across the 2–18 GHz frequency range. For measurement standardization, the composite powders were homogeneously blended with paraffin at a 1 : 1 mass ratio and subsequently pressed into toroidal specimens with defined geometry (outer diameter: 7 mm, inner diameter: 3 mm, thickness: 3 mm).

3. Results and discussions

3.1 Characterization of sample

The morphology and the structure of the samples were investigated by TEM (Fig. 2) and FE-SEM (Fig. 3). As revealed in Fig. 2a, the pristine $CoFe_2O_4$ nanoparticles exhibit well-defined spherical morphology with uniform size distribution and minimal particle aggregation. As a comparison, Fig. 2b demonstrates successful integration of numerous $CoFe_2O_4$ nanoparticles with irregular morphology onto RGO sheets. The RGO substrate displays characteristic two-dimensional sheet morphology with distinct surface wrinkling, a typical feature of graphene-based materials. After being coated with SiO_2 (Fig. 2c), the spherical morphology of $CoFe_2O_4$ nanoparticles remain unchanged, but the dispersibility of the particles sharply decreases, which may be due to the existence of a large number of hydroxyl and unsaturated residual bonds on the

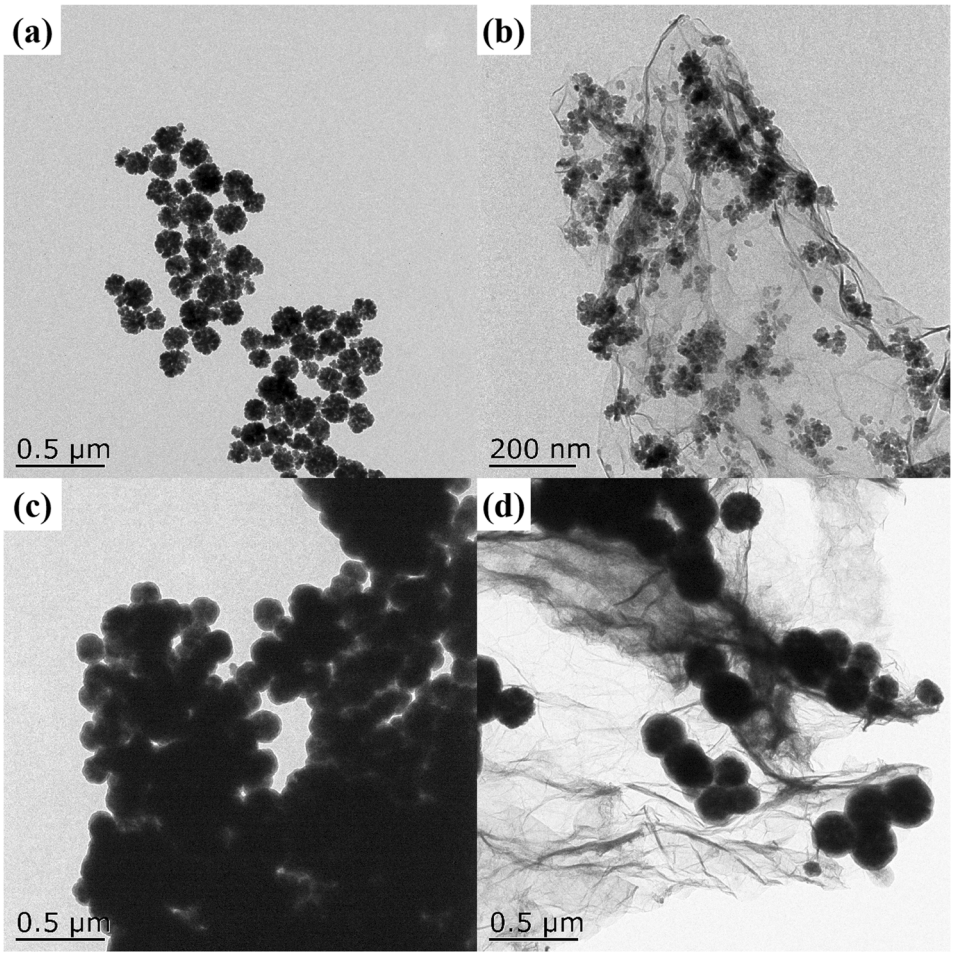

Fig. 2 TEM images of (a) $CoFe_2O_4$, (b) $CoFe_2O_4$/RGO, (c) $CoFe_2O_4$@SiO_2 and (d) $CoFe_2O_4$@SiO_2/RGO composites.

surface of silica, and the high surface energy is easy to promote the particles to form aggregates through van der Waals force or hydrogen bond. Differently, as shown in Fig. 2d, when $CoFe_2O_4$@SiO_2 particles are combined with RGO, the dispersibility is greatly improved. It can be seen that RGO can effectively reduce the agglomeration between $CoFe_2O_4$@SiO_2 nanoparticles. This also confirmed the successful preparation of $CoFe_2O_4$@SiO_2/RGO composites. The characterization results obtained from FE-SEM also support these findings. And the EDS elemental mapping confirms homogeneous distribution of Co, Fe, C, Si and O within the $CoFe_2O_4$@SiO_2/RGO composites. All these confirmed that the composite nanomaterials were successfully prepared by the designed experimental route.

The crystal structure of RGO, $CoFe_2O_4$, $CoFe_2O_4$/RGO, $CoFe_2O_4$@SiO_2 and $CoFe_2O_4$@SiO_2/RGO were recorded by XRD analysis. As shown in Fig. 4a, the diffraction peaks observed at 2θ = 18.3°, 30.1°, 35.3°, 43.1°, 53.5°, 57.0° and 62.3° corresponded to the (111), (220), (311), (400), (422), (511), and (440) crystallographic planes of cubic spinel-type $CoFe_2O_4$ (JCPDS 22-1086).[31] After being coated with SiO_2 and compounded with RGO, the characteristic peak of $CoFe_2O_4$ still existed, indicating that the composite process would not damage the crystal structure of $CoFe_2O_4$. Notably, the absence of distinct SiO_2 diffraction peaks in the XRD pattern of $CoFe_2O_4$@SiO_2 and $CoFe_2O_4$@SiO_2/RGO confirmed its amorphous nature, which aligned with the sol–gel synthesis process involving TEOS hydrolysis and condensation. The characteristic diffraction peak of RGO (typically at ~25°) also did not appear in the XRD spectra of $CoFe_2O_4$/RGO and $CoFe_2O_4$@SiO_2/RGO, may be due to the dominant diffraction intensity of highly crystalline $CoFe_2O_4$ nanoparticles and the effective exfoliation of graphene layers during the formation of the composite. These results collectively confirmed the successful preparation of $CoFe_2O_4$@SiO_2/RGO composites with well-defined structural features.

The microstructure changes of carbon materials during chemical reaction can be characterized by Raman spectroscopy. Fig. 4b shows the Raman spectra of GO, RGO, $CoFe_2O_4$/RGO and $CoFe_2O_4$@SiO_2/RGO composites in the range of 1000–2000 cm^{-1}, respectively. The Raman spectrum of GO exhibits two distinct peaks: the D-band peak at 1350 cm^{-1} and the G-band peak at 1600 cm^{-1}. Among them, the D-band peak is generated by the defects in the graphite and the graphite edge, while the G-band peak is generated by the symmetric vibration of sp^2 hybrid carbon atoms in the same plane.[32] However, compared with GO, it can be found that the G-band peak of RGO is shifted from 1600 cm^{-1} to 1582 cm^{-1}, while the intensity of D-

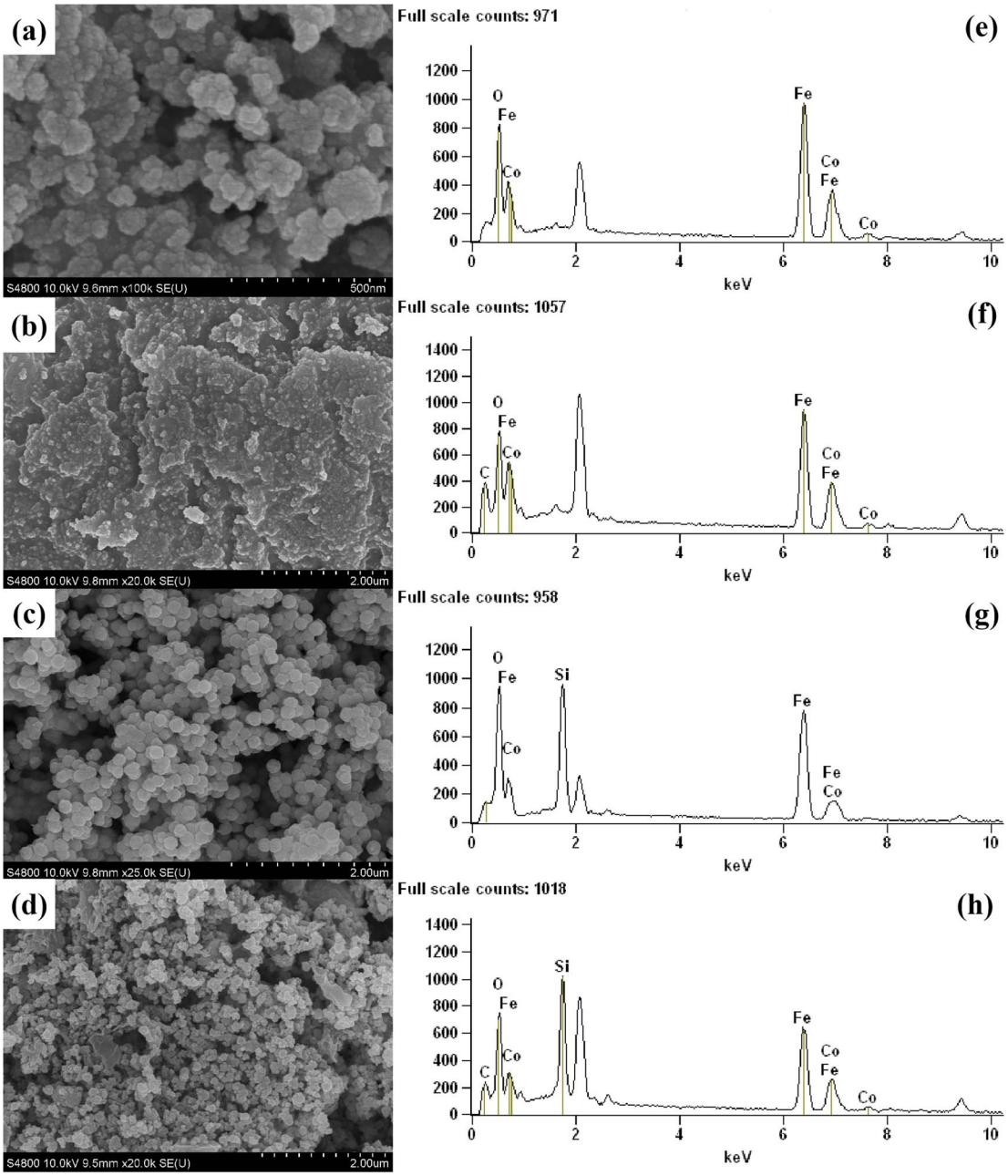

Fig. 3 SEM images of (a) $CoFe_2O_4$, (b) $CoFe_2O_4$/RGO, (c) $CoFe_2O_4$@SiO_2 and (d) $CoFe_2O_4$@SiO_2/RGO composites and (e–h) the corresponding EDS spectra.

band peak is significantly increased, indicating that GO is successfully reduced to RGO. In addition, the strength ratio (I_D/I_G) was used to estimate the degree of defect. The strength ratio of $CoFe_2O_4$@SiO_2/RGO composite ($I_D/I_G = 1.36$) and $CoFe_2O_4$/RGO composite ($I_D/I_G = 1.25$) were both higher than that of GO ($I_D/I_G = 0.94$). This shows that the average size of sp^2 domain decreases, and the disorder and defects increase after GO is reduced to RGO by hydrazine hydrate. In addition, it can be seen that there are more defects and disorder in $CoFe_2O_4$@SiO_2/RGO composites.[33–35]

It is well known that magnetic properties are useful for the analysis of electromagnetic absorption. Fig. 5 shows the room temperature hysteresis loops of the prepared $CoFe_2O_4$, $CoFe_2O_4$/RGO, $CoFe_2O_4$@SiO_2 and $CoFe_2O_4$@SiO_2/RGO nanoparticles in the range of −20 kOe to 20 kOe. With the introduction of RGO and the coating of SiO_2, the magnetization of $CoFe_2O_4$ decreases gradually. The corresponding data are presented in Table 1. It can be seen from Table 1 that the saturation magnetization (M_s) of $CoFe_2O_4$, $CoFe_2O_4$/RGO, $CoFe_2O_4$@SiO_2 and $CoFe_2O_4$@SiO_2/RGO are 77.8, 72.6, 50.4 and 49.6 emu g^{-1}, respectively. This indicates that the M_s of the nanocomposite is attributable to its magnetic composition, the increase of non-magnetic SiO_2 and RGO in the composites would reduce the content of $CoFe_2O_4$, resulting in a significant decrease in M_s of

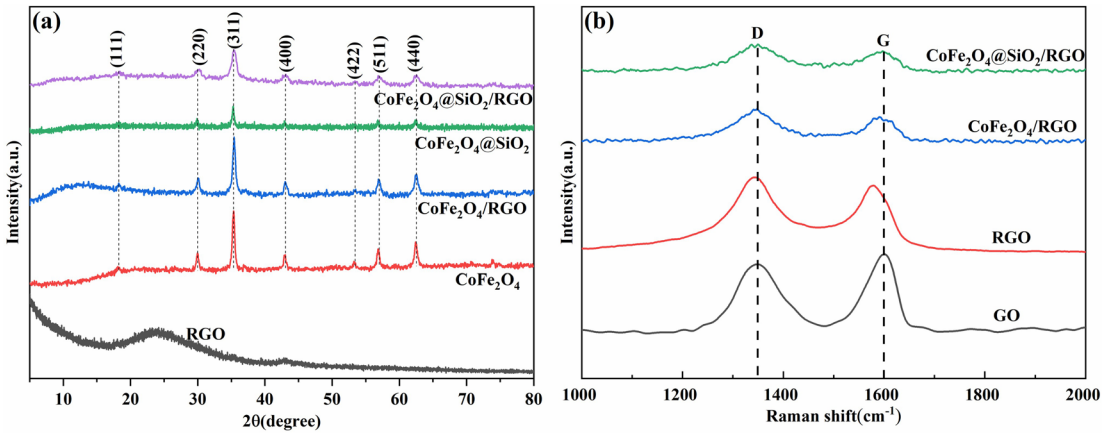

Fig. 4 (a) XRD spectra of RGO, $CoFe_2O_4$, $CoFe_2O_4$/RGO, $CoFe_2O_4$@SiO_2 and $CoFe_2O_4$@SiO_2/RGO nanocomposites and (b) Raman spectra of GO, RGO, $CoFe_2O_4$/RGO and $CoFe_2O_4$@SiO_2/RGO nanocomposites.

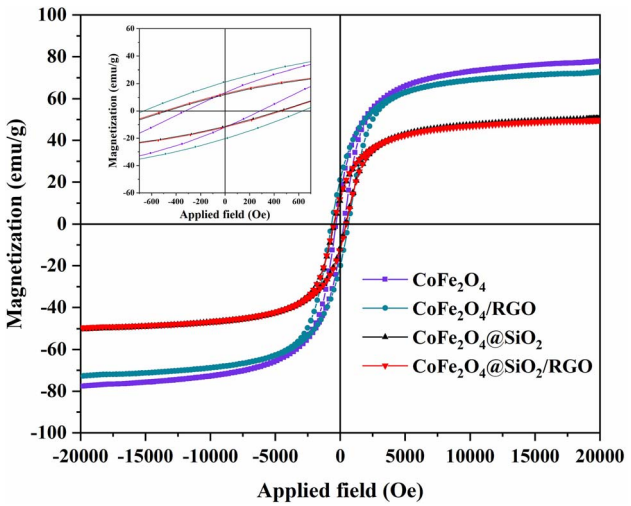

Fig. 5 VSM measurement results of $CoFe_2O_4$, $CoFe_2O_4$/RGO, $CoFe_2O_4$@SiO_2, $CoFe_2O_4$@SiO_2/RGO nanocomposites.

Table 1 Magnetic parameters of the different samples

Sample	M_s (emu g^{-1})	M_r (emu g^{-1})	H_c (Oe)
$CoFe_2O_4$	77.8	13.8	310.1
$CoFe_2O_4$/RGO	72.6	20.3	629.3
$CoFe_2O_4$@SiO_2	50.4	11.8	446.9
$CoFe_2O_4$@SiO_2/RGO	49.6	12.7	474.2

$CoFe_2O_4$@SiO_2/RGO composites.[36] In addition, the remanent magnetization (M_r) values measured for the nanocomposites were found to be 13.8 emu g^{-1} for $CoFe_2O_4$, 20.3 emu g^{-1} for $CoFe_2O_4$/RGO, 11.8 emu g^{-1} for $CoFe_2O_4$@SiO_2, and 12.7 emu g^{-1} for the $CoFe_2O_4$@SiO_2/RGO, substantiating that all materials retain substantial magnetic properties even in the absence of an applied magnetic field. Remarkably, a significant enhancement in H_c was observed after compounding with other components, suggesting that increased magnetic anisotropy promotes higher resonance frequency in electromagnetic fields.[37] However, both $CoFe_2O_4$@SiO_2 and $CoFe_2O_4$@SiO_2/RGO composites exhibited reduced H_c values compared to $CoFe_2O_4$/RGO without SiO_2. This phenomenon could be attributed to the multifaceted influences of particle size distribution, surface anisotropy modulation, and interfacial crystal interactions on coercivity.[38,39] Intriguingly, the $CoFe_2O_4$@SiO_2/RGO demonstrated marginally higher H_c than the $CoFe_2O_4$@SiO_2. This subtle enhancement might originate from the synergistic integration of $CoFe_2O_4$, SiO_2 and RGO during synthesis, which potentially amplifies surface anisotropy at interfacial regions within the composite architecture.

3.2 EMW absorbing properties

It is known that complex permittivity (ε' and ε'') and complex permeability (μ' and μ'') are the key electromagnetic parameters to characterize the wave-absorbing properties of materials. The real part of the complex permittivity (ε') and the complex permeability (μ') indicates the storage capacity of electrical and magnetic energy, while the imaginary part (ε'' and μ'') indicates the loss capacity of electrical and magnetic energy. The primary factors contributing to energy dissipation within materials encompass conduction, resonance, and relaxation phenomena. The loss mechanism inherent in electromagnetic absorbers is delineated by the attenuation mechanism of EMW, which is quantitatively assessed through the dielectric tangent loss ($\tan \delta_\varepsilon = \varepsilon''/\varepsilon'$) and the magnetic tangent loss ($\tan \delta_\mu = \mu''/\mu'$) associated with the absorber materials.[40] As illustrated in Fig. 6a, both $CoFe_2O_4$ and $CoFe_2O_4$@SiO_2 nanoparticles demonstrate stable ε' values of 4.5 ± 0.2 and 3.0 ± 0.1, respectively, over the frequency range of 2–18 GHz. In contrast, the $CoFe_2O_4$/RGO and $CoFe_2O_4$@SiO_2/RGO composites maintain significantly enhanced ε' values after compounding with RGO. What's more, the both composites demonstrate pronounced frequency-dependent dielectric responses, with their ε' values decreasing progressively from 12.6 to 7.5 and 15.4 to 8.6, respectively. Complementary observations are evident in the ε'' data presented in Fig. 6b. The ε'' values for $CoFe_2O_4$/RGO and

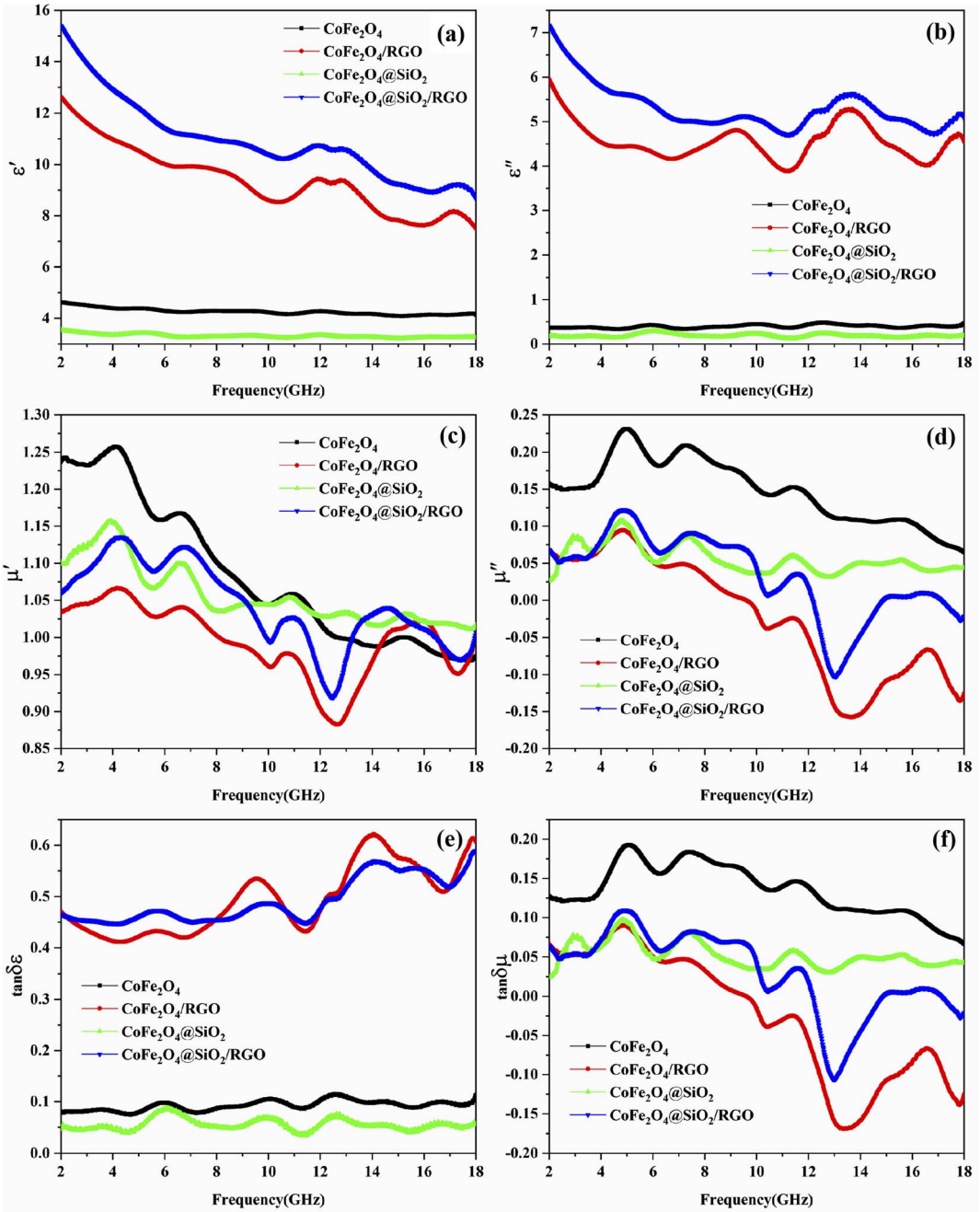

Fig. 6 Frequency dependence of (a) the real part of complex permittivity ε', (b) the imaginary part of complex permittivity ε'', (c) the real part of complex permeability μ', (d) the imaginary part of complex permeability μ'', (e) dielectric loss tan δ_ε and (f) magnetic loss tan δ_μ of $CoFe_2O_4$, $CoFe_2O_4$/RGO, $CoFe_2O_4$@SiO_2 and $CoFe_2O_4$@SiO_2/RGO nanocomposites.

$CoFe_2O_4$@SiO_2/RGO composites range from 4.2–5.9 and 4.7–7.1, respectively, representing 1.5–2.3 times enhancement over the base nanoparticles. This systematic improvement in both ε' and ε'' components can be principally attributed to the incorporation of RGO. The two-dimensional carbon network introduces enhanced charge carrier mobility and interfacial polarization effects, as described by the relationship:

$$\varepsilon_r = \varepsilon' - j\varepsilon'' = \left(\varepsilon_\infty + \frac{\sigma}{j\omega\varepsilon_0}\right) + \chi_e + \chi_d$$

where ε_r is the relative complex permittivity, j is the imaginary number with $\sqrt{-1}$ value,[41] ω is the angular frequency, ε_∞ and ε_0 are the relative dielectric permittivity at high-frequency limit and dielectric constant in a vacuum, respectively, σ represents conductivity, χ_e denotes electronic polarization, and χ_d accounts for dipole polarization. The RGO component elevates electronic polarization through its high electron density states while simultaneously improving interfacial charge transport, thereby synergistically enhancing the overall complex permittivity characteristics of the composite systems.[42] As shown in

Fig. 6c and d, the $CoFe_2O_4$@SiO_2/RGO composite exhibits relative complex permeability parameters μ' and μ'' ranging from 0.91 to 1.14 and −0.17 to 0.12, respectively, within the 2–18 GHz frequency range. A striking observation is that both the μ' and μ'' components of complex permeability demonstrate significant enhancement compared to the $CoFe_2O_4$/RGO composite. Notably, the negative imaginary part of permeability observed in Fig. 6d originates from the eddy-current-driven magnetic energy effect in highly conductive composites at high frequencies. The incorporation of RGO nanosheets significantly enhances the composite's electrical conductivity, causing the eddy currents to radiate magnetic energy back into space.[43] Remarkably, both $CoFe_2O_4$/RGO and $CoFe_2O_4$@SiO_2/RGO composites maintain electromagnetic wave absorption capabilities in this high-frequency regime despite the negative μ'' values. This apparent contradiction can be explained by the interference effect occurring at the air-sample interface, where the 180° phase difference between incident and reflected electromagnetic waves leads to destructive interference, thereby suppressing wave reflection. The coexistence of negative permeability and absorption performance demonstrates the complex interplay between intrinsic material properties and wave interference phenomena in these advanced absorbing materials. Comparative analysis of Fig. 6e and f reveals a distinct dielectric dominance in EMW absorption, evidenced by the tan δ_ε values substantially exceeding those of tan δ_μ. This pronounced disparity confirms that dielectric loss constitutes the primary attenuation mechanism for EMW in the $CoFe_2O_4$@SiO_2/RGO composite throughout the investigated frequency spectrum.

Comparative analysis reveals that the strategic integration of RGO nanosheets into $CoFe_2O_4$/RGO and $CoFe_2O_4$@SiO_2/RGO significantly enhances the electronic polarization degree and electrical conductivity. This synergistic effect ultimately leads to substantial improvement in EMW absorption performance. It is particularly noteworthy that while the SiO_2 coating layer on $CoFe_2O_4$@SiO_2 diminishes their magnetic energy-loss capacity in comparison to $CoFe_2O_4$, the optimized $CoFe_2O_4$@SiO_2/RGO composite demonstrates balanced electromagnetic energy dissipation through rational regulation of magnetic loss characteristics. Specifically, the reduced disparity between dielectric loss and magnetic loss enables better impedance matching, while the insulating SiO_2 interlayer effectively suppresses eddy current effects at high frequencies.[44] This dual mechanism not only minimizes electromagnetic wave reflection at the material–air interface but also facilitates enhanced electromagnetic energy conversion within the absorber, ultimately contributing to superior electromagnetic wave attenuation performance.

It is widely recognized that the dielectric loss mechanism in materials primarily stems from two main sources: conduction loss and polarization loss. Upon incorporation of RGO, the continuous conductive network formed by RGO generates significant Joule heating *via* charge carrier migration, constituting the conduction loss. On the other hand, the presence of chemical dangling bonds, lattice distortions at the $CoFe_2O_4$@SiO_2 interfaces, and inherent defects within the RGO structure (such as fractures in sp^2-hybridized carbon domains) effectively induce strong interfacial polarization and dipolar relaxation, forming the crucial polarization loss mechanism.[45,46] These phenomena are experimentally corroborated by the distinct Cole–Cole semicircular features observed in Fig. 7a. The Cole–Cole plot of the $CoFe_2O_4$@SiO_2/RGO composite exhibits multiple semicircular arcs, indicative of superimposed polarization relaxation mechanisms. This multi-relaxation behavior facilitates efficient electromagnetic energy dissipation through various polarization conversion pathways, thereby significantly improving the composite's EMW absorption capabilities.[47] Furthermore, the characteristic linear tail of the Cole–Cole curve provides direct evidence of conduction loss contributions. The synergistic combination of these polarization and conduction mechanisms establishes an optimized dielectric loss environment for enhanced microwave absorption performance. Magnetic loss mechanisms in electromagnetic wave absorbers mainly arise from natural resonance, exchange resonance, and eddy current effects, with distinct mechanisms dominating at specific frequency ranges. Analysis of the magnetic loss mechanisms in electromagnetic wave absorbing materials, particularly through frequency-dependent studies of the eddy current coefficient C_0 ($C_0 = \mu''(\mu')^{-2} \times f^{-1}$, f is the frequency of EMW), elucidates the dominant attenuation pathways. As depicted in Fig. 7b, the C_0 values of the $CoFe_2O_4$@SiO_2/RGO composite exhibit a significant frequency-dependent decline across 2–18 GHz, definitively excluding eddy current loss as the primary mechanism.[48] This phenomenon arises from the electrically insulating SiO_2 interlayer, which effectively suppresses eddy current generation at the $CoFe_2O_4$/RGO interfaces, thereby markedly reducing detrimental electromagnetic coupling effects. This suppression aligns with the characteristic resonance peaks observed in the μ'' spectrum. Notably, while the C_0 values of pure $CoFe_2O_4$ and $CoFe_2O_4$/RGO display persistent fluctuations within this frequency band (reflecting competitive coexistence of multi-mechanisms such as natural resonance and exchange resonance), the C_0 values of $CoFe_2O_4$@SiO_2 demonstrate clear stabilization beyond 12 GHz. This stability indicates that in high-frequency regions, the thorough inhibition of eddy currents by the SiO_2 interlayer enables residual magnetic loss mechanisms (*e.g.* natural resonance) to predominantly govern attenuation. The frequency independence of C_0 at these frequencies validates the signature trait of resonance-dominated loss. Consequently, the interfacial insulation design effectively optimizes high-frequency magnetic loss performance by selectively suppressing eddy current loss.

The electromagnetic energy dissipation capacity of the composite was quantitatively evaluated using the attenuation constant (α), derived from transmission line theory, which can be expressed as follows:

$$\alpha = \frac{\sqrt{2}}{c}\pi f\sqrt{\left(\varepsilon''\mu'' - \varepsilon'\mu'\right) + \sqrt{\left(\varepsilon''\mu'' - \varepsilon'\mu'\right)^2 + \left(\varepsilon''\mu' + \varepsilon'\mu''\right)^2}}$$

where c is the velocity of light, f is the frequency of EMW. As demonstrated in Fig. 7c, the $CoFe_2O_4$@SiO_2/RGO composite exhibits superior α values across the 2–18 GHz spectrum compared to control materials. This enhanced attenuation

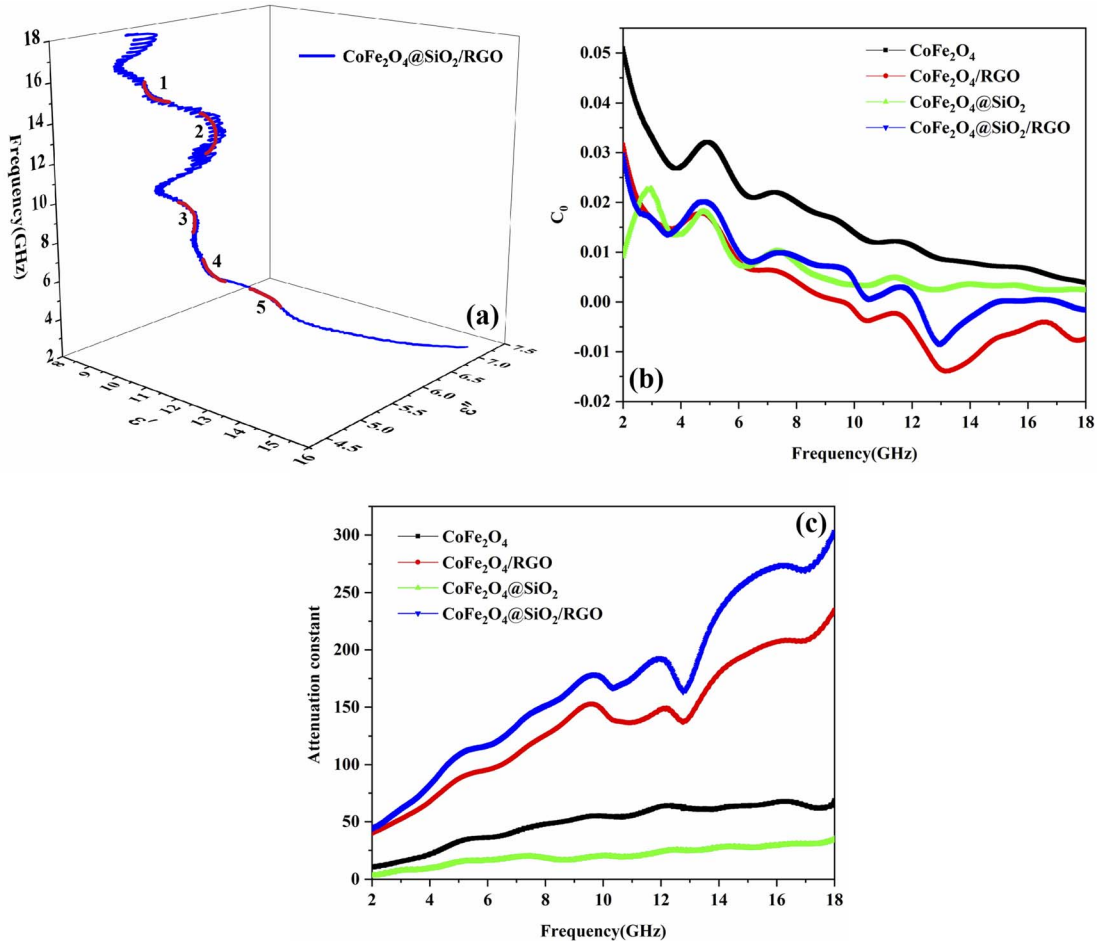

Fig. 7 (a) Typical Cole–Cole semicircles, (b) C_0 (representing eddy current loss) *versus* frequency of $CoFe_2O_4$, $CoFe_2O_4$/RGO, $CoFe_2O_4$@SiO_2 and $CoFe_2O_4$@SiO_2/RGO nanocomposites, and (c) attenuation constant of $CoFe_2O_4$, $CoFe_2O_4$/RGO, $CoFe_2O_4$@SiO_2 and $CoFe_2O_4$@SiO_2/RGO nanocomposites.

capability directly correlates with the composite's optimized impedance matching and synergistic multi-loss mechanisms, including interfacial polarization, magnetic resonance, and conductive network effects. The maximized α values confirm that the hierarchical heterostructure design effectively converts incident electromagnetic energy into thermal dissipation through coupled dielectric–magnetic interactions, thereby achieving exceptional EMW absorption performance.

In order to further reveal the absorption characteristics of EMWs, the RL was calculated according to the transmission line theory, with the relevant formulas presented below (1) and (2):

$$\mathrm{RL} = 20 \log \left| \frac{Z_{\mathrm{in}} - Z_0}{Z_{\mathrm{in}} + Z_0} \right| \quad (1)$$

$$Z_{\mathrm{in}} = Z_0 \sqrt{\mu_{\mathrm{r}}/\varepsilon_{\mathrm{r}}} \tanh \left[\mathrm{j} \left(\frac{2\pi f d}{c} \right) \sqrt{\mu_{\mathrm{r}} \varepsilon_{\mathrm{r}}} \right] \quad (2)$$

where Z_{in} represents the input impedance of absorber and Z_0 is the impedance of free space, f denotes the frequency of EMW, d is the thickness of absorbing layer, c stands for the velocity of EMW in vacuum, tanh represents the hyperbolic tangent function, which describes the reflection and transmission characteristics of EMW when they propagate through a medium, while ε_{r} and μ_{r} are the relative complex permittivity and permeability, respectively. Fig. 8 presents the calculation results of reflection losses for $CoFe_2O_4$, $CoFe_2O_4$/RGO, $CoFe_2O_4$@SiO_2 and $CoFe_2O_4$@SiO_2/RGO composites. Pure $CoFe_2O_4$ nanoparticles exhibited limited electromagnetic wave absorption performance, with RL values remaining above the −10 dB threshold required for practical applications (Fig. 8a and e). The integration of RGO significantly enhanced the absorption properties. The $CoFe_2O_4$/RGO composite demonstrated a remarkable minimum RL of −59.2 dB at 11.32 GHz, with an absorber thickness of 2.3 mm (as shown in Fig. 8b and f). Nevertheless, this composite displayed a relatively narrow effective absorption bandwidth (RL ≤ −10 dB) spanning only 2.92 GHz from 10.08 GHz to 13 GHz, indicating potential for bandwidth optimization through structural modifications. Interestingly, the surface modification with silica brought about distinct changes in performance. The $CoFe_2O_4$@SiO_2 nanoparticles showed inadequate EMW attenuation capabilities, achieving only a minimal RL of −3.08 dB (Fig. 8c and g). These results underscore the critical influence of composite architecture on EMW absorption efficiency. The most remarkable

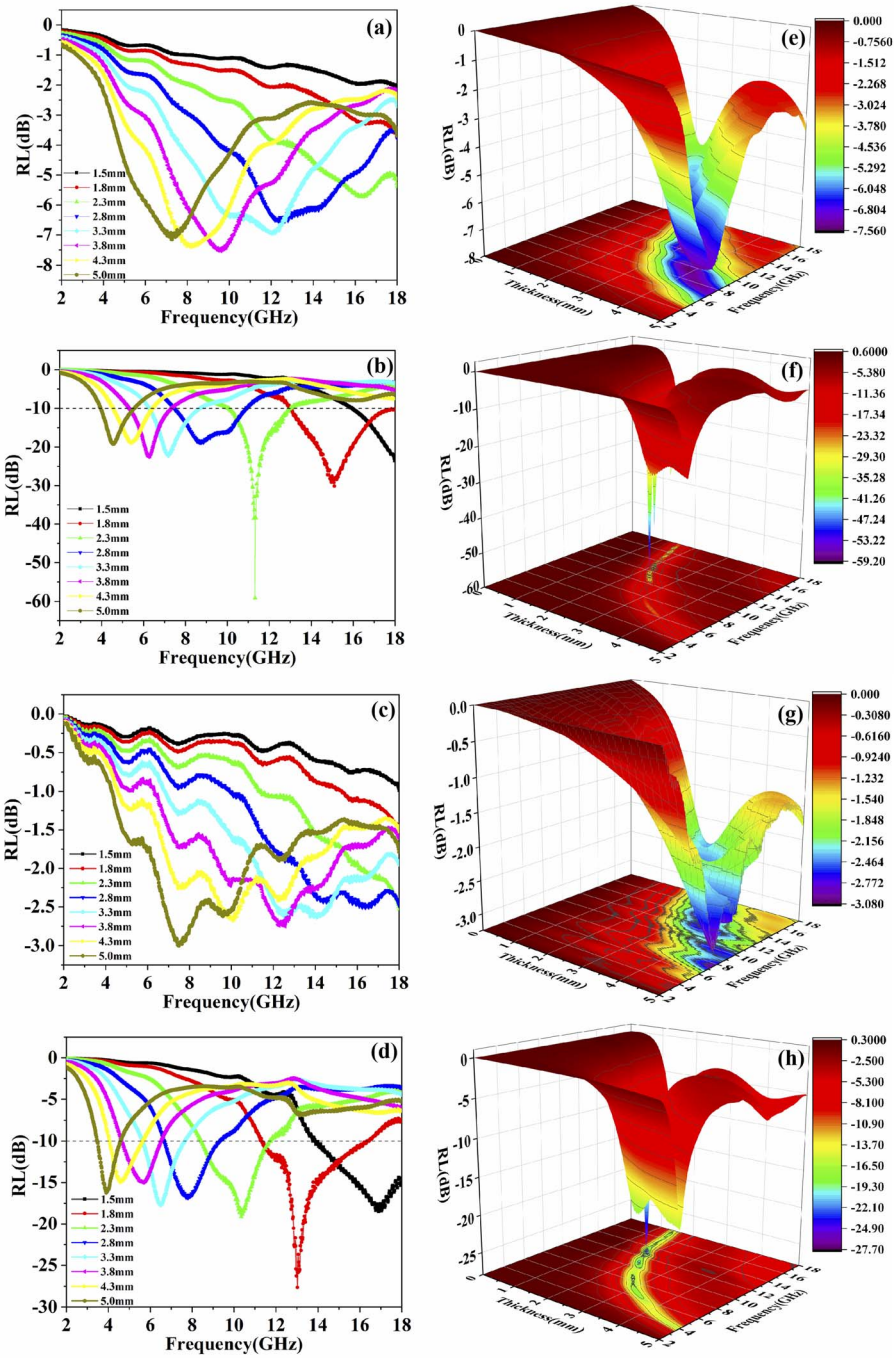

Fig. 8 Reflection loss curves of (a) $CoFe_2O_4$, (b) $CoFe_2O_4$/RGO, (c) $CoFe_2O_4$@SiO_2 and (d) $CoFe_2O_4$@SiO_2/RGO composites with a thickness in the range of 1.5–5.0 mm, and (e–h) the corresponding three dimensional presentation.

improvement in performance was observed in the ternary $CoFe_2O_4$@SiO_2/RGO composite (Fig. 8d and h). This optimized material exhibited exceptional broadband absorption characteristics, achieving a minimum RL of −27.7 dB at 13.02 GHz with a thin absorption layer thickness of just 1.8 mm. The composite demonstrated an effective absorption bandwidth (RL $\leq$ −10 dB) of 5 GHz from 11.32 GHz to 16.32 GHz at optimal thickness. When the thickness was adjusted from 1.5 mm to 5 mm, the absorption bandwidth expanded significantly to 14.52 GHz (3.48–18 GHz), achieving full-frequency coverage from S-band to Ku-band. This exceptional broadband absorption performance outperforms that of the other tested composites, suggesting synergistic effects between the SiO_2 coating and RGO matrix that enhance impedance matching and electromagnetic energy dissipation. The thickness-dependent absorption characteristics reveal tunable microwave absorption capabilities, positioning this composite as a promising candidate for advanced electromagnetic shielding applications. These

findings provide a valuable guide for designing high-efficiency microwave absorbers by employing rational composite engineering approaches.

To elucidate the physical phenomenon and the underlying mechanism behind the enhanced electromagnetic wave absorption performance of $CoFe_2O_4$@SiO_2/RGO composites, the experimental data were scrutinized by using the quarter-wave thickness criterion.[49] In this criterion, when the thickness (t_m) of the composite meets the matching eqn (3), the RL is maximum at a certain electromagnetic wave frequency (f_m),[50]

$$t_m = \frac{nc}{4f_m\sqrt{|\mu_r||\varepsilon_r|}} \quad (n = 1, 3, 5, \ldots) \tag{3}$$

where $|\varepsilon_r|$ and $|\mu_r|$ denote the measured moduli of ε_r and μ_r at the frequency f_m, respectively. As demonstrated in Fig. 9b, the experimental absorber thickness values (t_m^{exp}) corresponding to maximum RL peaks (Fig. 9a) for the $CoFe_2O_4$@SiO_2/RGO composite exhibit remarkable alignment with the theoretical quarter-wave thickness criterion matching curves. In addition, the RL is intimately linked to the impedance matching characteristics, which can be quantified by the normalized impedance matching characteristic modulus $Z = |Z_{in}/Z_0|$ (formula (4)). This parameter plays a crucial role in minimizing electromagnetic wave reflection at the absorber–air interface.[51]

$$Z = \left|\frac{Z_{in}}{Z_0}\right| = \sqrt{\left|\frac{\mu_r}{\varepsilon_r}\right|}\tanh\left[j\left(\frac{2\pi fd}{c}\right)\sqrt{\mu_r\varepsilon_r}\right] \tag{4}$$

When the value of Z approaches or is nearly equal to 1, the absorber exhibits favorable impedance matching characteristics. This enables incident EMWs to penetrate easily into the absorber, where they are subsequently attenuated rather than being reflected back to the absorber's surface. Consequently, the EMWs are transformed into heat energy or dissipated through interference effects.[52,53] Fig. 9c illustrates the frequency dependent behavior of the Z for the $CoFe_2O_4$@SiO_2/RGO composite. Based on the quarter-wave thickness criterion, it was evident that when the absorber had a thickness of 1.8 mm, the Z value at the frequency of 13.02 GHz closely approached 1. At this specific condition, the RL reached its minimum value of −27.7 dB. This indicates that a well-matched characteristic impedance plays a significant role in enhancing the EMW absorption performance of $CoFe_2O_4$@SiO_2/RGO composite.

Based on the above comprehensive analysis, Fig. 10 schematically presents a plausible illustration of the EMW absorption mechanism operating within the $CoFe_2O_4$@SiO_2/RGO composite. Firstly, the hierarchical structure design extends attenuation performance through multiple physical mechanisms: the two-dimensional wrinkled skeleton of RGO forms a large-scale conductive network, prolonging the electromagnetic wave propagation path.[54] Simultaneously, the SiO_2 dielectric spacer layer establishes a gradient dielectric distribution, promoting wavefront scattering and multiple reflections. This "core–shell–substrate" sandwich structure achieves dual optimization. Macroscopically, the large-pore structure of the RGO sheets optimizes the material–air interface impedance matching. Microscopically, the micro-interfaces of the $CoFe_2O_4$@SiO_2 core–shell units provide high-density polarization sites; their relaxation frequency covers the S–Ku bands (2–18 GHz), forming spectral complementarity with the magnetic loss component.[55] Moreover, the multifaceted attenuation mechanisms integrate conductive dissipation through RGO's electron transport network with dielectric relaxation processes, while magnetic resonance phenomena from $CoFe_2O_4$ nanocrystals simultaneously induce eddy current and natural resonance losses. Particularly, the ternary interface engineering between core–shell $CoFe_2O_4$@SiO_2 and RGO substrates establishes gradient dielectric distributions, promoting intensive interfacial polarization accumulation and defect-induced dipole alignment at heterojunction boundaries. These synergistic polarization-dominant losses coupled with optimized impedance matching collectively enable deep electromagnetic energy penetration and *in situ* conversion.[56] Secondly, the hierarchical

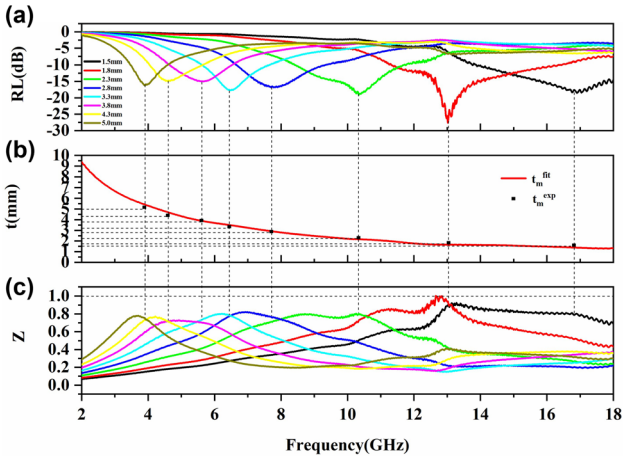

Fig. 9 (a) Frequency dependence of the RL with different thicknesses, (b) the simulations of the absorber thickness (t_m) *versus* peak frequency (f_m) under quarter-wave thickness criterion, and (c) the relationship between the impedance matching characteristics ($Z = |Z_{in}/Z_0|$) and the EMW frequency of $CoFe_2O_4$@SiO_2/RGO composite.

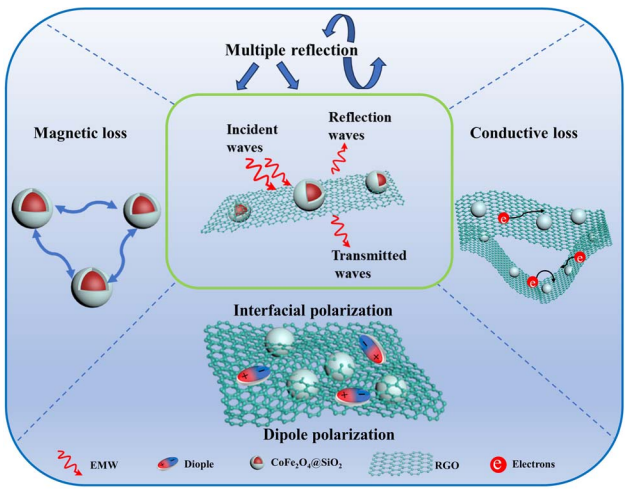

Fig. 10 Schematic of the EMWs absorbing mechanisms in $CoFe_2O_4$@SiO_2/RGO composites.

core–shell architecture facilitates multistage wave–matter interactions *via* (i) geometrically prolonged propagation trajectories through layered RGO substrates, (ii) wavefront scattering at SiO_2 dielectric spacers, and (iii) repetitive reflection/refraction cycles within the spherical $CoFe_2O_4$@SiO_2 units. This hierarchical confinement paradigm effectively prolongs microwave dwell time while activating interfacial polarization relaxation processes across dimensional gradients.[57] Thirdly, the ferromagnetic $CoFe_2O_4$ components induce dual resonance effects: natural resonance phenomena under GHz-frequency excitation and exchange resonance effects arising from intergranular spin interactions, both augmenting magnetic hysteresis losses through enhanced permeability dispersion.[58] The hierarchical heterostructure of $CoFe_2O_4$@SiO_2/RGO composite thus achieves synergistic combination of complementary loss mechanisms ultimately yielding an ultrathin absorber with exceptional absorption intensity and broad effective bandwidth.

4. Conclusion

This study demonstrates the successful fabrication of multilayered $CoFe_2O_4$@SiO_2/RGO composite through a facile method of electrostatic self-assembly. The rational integration of core–shell $CoFe_2O_4$@SiO_2 microspheres with RGO nanosheets established a ternary synergistic system, where magnetic–dielectric–conductive components collectively enhanced EMW absorption. Particularly, the optimized composite exhibited remarkable absorption performance at ultrathin thickness (1.8 mm), achieving a minimum RL of −27.7 dB at 13.02 GHz with an effective absorption bandwidth (RL ≤ −10 dB) spanning 5.0 GHz (11.32–16.32 GHz). Consequently, these attributes collectively position $CoFe_2O_4$@SiO_2/RGO as a material with extensive application potential, spanning from military equipment, where its EMW absorbing capabilities can enhance stealth and electromagnetic compatibility, to civil health products, such as shielding materials for electronic devices to safeguard human health against electromagnetic radiation.

Data availability

The data that support the findings of this study are available from the corresponding author upon reasonable request.

Conflicts of interest

There are no conflicts of interest to declare.

Acknowledgements

The authors are grateful for the National Nature Science Foundation of China (no. 51902141), the Natural Science Foundation of Jiangsu Province (no. BK20191038), the "Qinglan Project" of Jiangsu Universities of Jiangsu Province, the "Unveiling the List and Entrusting the Leader" Scientific and Technological Research Project in Zhonglou District of Changzhou.

References

1 W. Bao, C. Chen, W. Chen, X. Ding and Z. Si, *J. Mater. Sci.: Mater. Electron.*, 2020, **31**, 12775–12782.
2 S. Zhou, D. Liu, K. Fan, H. Liu and X. Zhang, *Nanoscale*, 2024, **16**, 18644–18665.
3 G. Dai, R. Deng, X. You, T. Zhang, Y. Yu and L. Song, *J. Mater. Sci. Technol.*, 2022, **116**, 11–21.
4 M. Ma, Y. Bi, Z. Tong, Y. Liu, P. Lyu, R. Wang, Y. Ma, G. Wu, Z. Liao and Y. Chen, *RSC Adv.*, 2021, **11**, 16572–16591.
5 X. Jian, B. Wu, Y. Wei, S. Dou, X. Wang, W. He and N. Mahmood, *ACS Appl. Mater. Interfaces*, 2016, **8**, 6101–6109.
6 B. Dai, T. Qi, M. Song, M. Geng, Y. Dai and Y. Qi, *Nanoscale*, 2022, **14**, 10456–10468.
7 C. Jian, J. Zhang and X. Ma, *RSC Adv.*, 2020, **10**, 13277–13285.
8 Y. J. Zhang, Z. Zhang, S. Xu, L. Yu, Y. Long and Q. Tang, *RSC Adv.*, 2016, **6**, 6623–6630.
9 M. Liu, H. Huang, J. Mei, S. Yang, H. Tu and J. Wang, *J. Mater. Chem. A*, 2025, **13**, 1904–1914.
10 F. Li, W. Zhan, L. Zhuang, L. Zhou, M. Zhou, G. Bai, A. Zhou, W. Xiao, X. Yang and G. Sui, *J. Phys. Chem. C*, 2020, **124**, 14861–14872.
11 X. Liu, X. Cui, Y. Chen, X. Zhang, R. Yu, G. Wang and H. Ma, *Carbon*, 2015, **95**, 870–878.
12 J. Lu, P. Shen, W. Yao, C. Jiang and J. Xu, *Nanoscale Res. Lett.*, 2016, **11**, 141.
13 Q. He, Y. Wu, Y. Tian, G. Li, J. Liu, P. Deng and D. Chen, *Nanomaterials*, 2019, **9**, 115.
14 S. Fang, D. Huang, R. Lv, Y. Bai, Z. Huang, J. Gu and F. Kang, *RSC Adv.*, 2017, **7**, 25773–25779.
15 B. Quan, Y. Chen, Y. Wang, X. Lu, T. Guo, M. Zhang and X. Huang, *Carbon*, 2023, **206**, 392–401.
16 B. Quan, Y. Wang, Y. Chen, M. Zhang, J. Liu, Q. Jia, X. Lu, J. Chen and X. Huang, *J. Mater. Chem. A*, 2023, **11**, 3625–3631.
17 Y. Chen, B. Quan, J. Liu, X. Lu, L. Lin, G. Shao, Y. Wen, R. Jin, X. Shen and X. Huang, *ACS Appl. Mater. Interfaces*, 2025, **17**, 9748–9759.
18 L. Liu, C. Xu, Y. Yang, C. Fu, F. Ma, Z. Zeng and G. Wang, *Mater. Horiz.*, 2025, **12**, 64–91.
19 C. Wang, X. Han, P. Xu, X. Zhang, Y. Du, S. Hu, J. Wang and X. Wang, *Appl. Phys. Lett.*, 2011, **98**, 072906.
20 L. Wang, Y. Huang, X. Sun, H. Huang, P. Liu, M. Zong and Y. Wang, *Nanoscale*, 2014, **6**, 3157–3164.
21 X. Guan, J. Kuang, L. Yang, M. Lu and G. Wang, *ChemistrySelect*, 2019, **4**, 9516–9522.
22 M. Fu, Q. Jiao and Y. Zhao, *J. Mater. Chem. A*, 2013, **1**, 5577–5586.
23 X. Zhang, G. Wang, W. Cao, Y. Wei, J. Liang, L. Guo and M. Cao, *ACS Appl. Mater. Interfaces*, 2014, **6**, 7471–7478.
24 G. Qing, N. A. Magid and B. Reza, *J. Magn. Magn. Mater.*, 2021, **537**, 168181.
25 F. Wu, A. Xie, M. Sun, Y. Wang and M. Wang, *J. Mater. Chem. A*, 2015, **3**, 14358–14369.
26 J. Xiao, M. He, B. Zhan, H. Guo, J. Yang, Y. Zhang, X. Qi and J. Gu, *Mater. Horiz.*, 2024, **11**, 5874–5894.

27 Y. Pan, G. Wang and Y. Yue, *RSC Adv.*, 2015, **5**, 71718–71723.
28 M. Han, X. Yin, L. Kong, M. Li, W. Duan, L. Zhang and L. Cheng, *J. Mater. Chem. A*, 2014, **2**, 16403–16409.
29 H. Lv, Y. Guo, Y. Zhao, H. Zhang, B. Zhang, G. Ji and Z. Xu, *Carbon*, 2016, **110**, 130–137.
30 M. T. H. Aunkor, I. M. Mahbubul, R. Saidur and H. S. C. Metselaar, *RSC Adv.*, 2016, **6**, 27807–27828.
31 S. Khanahmadi and S. Masoudpanah, *Ceram. Int.*, 2024, **50**, 9779–9788.
32 A. C. Ferrari and D. M. Basko, *Nat. Nanotechnol.*, 2013, **8**, 235–246.
33 Y. Li, W. Gao, L. Ci, C. Wang and M. A. Pulickel, *Carbon*, 2010, **48**, 1124–1130.
34 G. Liu, W. Jiang, Y. Wang, S. Zhong, D. Sun, J. Liu and F. Li, *Ceram. Int.*, 2015, **41**, 4982–4988.
35 H. Moussa, E. Girot, K. Mozet, H. Alem, G. Medjahdi and R. Schneider, *Appl. Catal., B*, 2016, **185**, 11–21.
36 J. W. Liu, J. Cheng, R. Che, J. Xu, M. Liu and Z. Liu, *ACS Appl. Mater. Interfaces*, 2013, **5**, 2503–2509.
37 V. A. Orlov, G. S. Patrin and I. N. Orlova, *J. Exp. Theor. Phys.*, 2020, **131**, 589–599.
38 L. Li, K. Chen, H. Li, G. Tong, H. Qian and B. Hao, *J. Alloys Compd.*, 2013, **557**, 11–17.
39 M. A. Laguna-Marco, J. Sánchez-Marcos, N. Menéndez, J. Chaboy, E. Salas-Colera and C. Prieto, *Mater. Des.*, 2016, **93**, 388–396.
40 A. M. Adnan, W. Ding, U. R. Sajid, H. Ali, Y. C. Bian, Q. C. Liu and Z. G. Sheng, *Appl. Surf. Sci.*, 2021, **543**, 148785.
41 S. S. Birajdar, A. R. Deshmukh, A. C. Kumbharkhane and D. B. Suryawanshi, *Russ. J. Phys. Chem. B*, 2023, **17**, 990–995.
42 Y. Chen, Z. Zhang, X. Yin and F. Zhang, *Russ. J. Phys. Chem. B*, 2025, **19**, 171–192.
43 M. Zhang, Z. Jiang, X. Lv, X. Zhang, Y. Zhang, J. Zhang, L. Zhang and C. Gong, *J. Phys. D: Appl. Phys.*, 2020, **53**, 1–10.
44 X. Ling, K. Wang, W. Zhang, Y. Wu, Q. Jin and D. Zhang, *J. Colloid Interface Sci.*, 2022, **625**, 317–327.
45 J. Cui, X. Wang, L. Huang, C. Zhang, Y. Yuan and Y. Li, *Carbon*, 2022, **187**, 115–125.
46 B. Quan, W. Shi, S. J. H. Ong, X. Lu, P. L. Wang, G. Ji, Y. Guo, L. Zheng and Z. J. Xu, *Adv. Funct. Mater.*, 2019, **29**, 1901236.
47 B. Dai, J. Li, X. Liu, N. Wang, Y. Dai and Y. Qi, *Carbon*, 2022, **195**, 308–318.
48 P. Zhang, Y. Yao, W. Zhou, Y. Liu, X. Cao and Z. Zhang, *Nanomaterials*, 2022, **12**, 1089.
49 C. Feng, X. Liu, Y. Sun, C. Jin and Y. Lv, *RSC Adv.*, 2014, **4**, 22710–22715.
50 H. Guo, X. Wang, Q. Qian, F. Wang and X. Xia, *ACS Nano*, 2009, **3**, 2653–2659.
51 J. Y. Fang, T. Liu, Z. Chen, Y. Wang, W. Wei, X. Yue and Z. Jiang, *Nanoscale*, 2016, **8**, 8899–8909.
52 J. H. Bi, C. Lin, D. Lu, A. Chen and X. Meng, *J. Phys. Chem. Solids*, 2022, **164**, 110624.
53 B. Wang, Y. Ji, P. Mu, Y. Huo, J. Xiang, A. Nie, T. Xue, K. Zhai, Z. Liu and F. Wen, *Appl. Surf. Sci.*, 2022, **591**, 153176.
54 B. Quan, W. Gu, J. Sheng, X. Lv, Y. Mao, L. Liu, X. Huang, Z. Tian and G. Ji, *Nano Res.*, 2021, **14**, 1495–1501.
55 B. Quan, Y. Chen, L. Lin, X. Zhou, X. Lu, M. Zhang and X. Huang, *Nanoscale*, 2024, **16**, 4796.
56 M. Han, X. Yin and L. Kong, *J. Mater. Chem. A*, 2014, **2**, 16403–16409.
57 C. Li, S. Yu, S. Luo, W. Yang, Z. Ge, H. Huang, R. Sun and C. Wong, *RSC Adv.*, 2016, **6**, 36450–36458.
58 K. Zhang, J. Li, F. Wu, M. Sun, Y. Xia and A. Xie, *ACS Appl. Nano Mater.*, 2019, **2**, 315–324.